Journal of Power Sources 621 (2024) 235236

Contents lists available at ScienceDirect

Journal of Power Sources

journal homepage: www.elsevier.com/locate/jpowsour

# Probabilistic deconvolution of the distribution of relaxation times from multiple electrochemical impedance spectra

Adeleke Maradesa [a], Baptiste Py [a], Francesco Ciucci [b,c,*]

[a] Department of Mechanical and Aerospace Engineering, The Hong Kong University of Science and Technology, China
[b] University of Bayreuth, Electrode Design for Electrochemical Energy Systems, 95448, Bayreuth, Germany
[c] University of Bayreuth, Bavarian Center for Battery Technology (BayBatt), 95448, Bayreuth, Germany

## HIGHLIGHTS

- Enhances multi-spectra analysis using quasi-Gaussian process.
- Evaluates DRT inversion's credibility.
- Accurately recovers DRT from noisy data.
- Provides a unified probabilistic approach for DRT analysis.

## ARTICLE INFO

*Keywords:*
Electrochemical impedance spectroscopy
Distribution of relaxation times
Gaussian processes
Quasi-GP model
Fuel cells
Batteries

## ABSTRACT

Electrochemical impedance spectroscopy (EIS) is widely used to study the properties of electrochemical materials and systems. However, analyzing EIS data remains challenging. Among various analysis methods, the distribution of relaxation times (DRT) has emerged as a novel non-parametric approach capable of providing timescale information. Among the various DRT inversion methods, those based on Gaussian processes (GP) are particularly promising because they provide uncertainty estimates for both EIS and DRT. However, current GP-based DRT implementations can only handle one spectrum at a time. This work extends these models to allow concurrent analysis of multiple impedance spectra as a function of experimental conditions. The new method, called the quasi-Gaussian process distribution of relaxation times, treats the DRT as a GP with respect to the experimental state and as a finite approximation of a positively constrained GP with respect to timescales. This new DRT inversion approach is validated against noise-corrupted artificial EIS data and applied to experimental data, allowing us to expedite EIS data analysis of multiple EIS data from a probabilistic perspective.

## 1. Introduction

Electrochemical impedance spectroscopy (EIS) is a versatile characterization and diagnostic technique widely used in electrochemistry applications [1–4] to study batteries [5–8], fuel cells [7,9,10], solar cells [11,12], electrolyzers [13–15], and beyond [16–21]. The distribution of relaxation times (DRT) has recently emerged as a promising non-parametric approach to analyze impedance spectra [22,23] and has been applied to identify electrode processes [24,25], estimate battery state-of-health [26–29], and assess the performance of fuel cells [30,31]. Furthermore, the DRT has been used to develop equivalent circuit models without requiring prior circuit architecture information [32–35]. Assuming that the experimental impedance depends on both frequency, $f$, and an experimental state, $\boldsymbol{\psi}$,[1] the DRT impedance model, $Z_{\mathrm{DRT}}(f,\boldsymbol{\psi})$, can be expressed in terms of $f$ and $\boldsymbol{\psi}$ as shown:

$$Z_{\mathrm{DRT}}(f,\boldsymbol{\psi}) = i2\pi f L_0(\boldsymbol{\psi}) + R_\infty(\boldsymbol{\psi}) + \int_{-\infty}^{+\infty} \frac{\gamma(\log\tau,\boldsymbol{\psi})}{1+2\pi i f\tau}\, d\log\tau \tag{1}$$

* Corresponding author. University of Bayreuth, Bavarian Center for Battery Technology (BayBatt), 95448, Bayreuth, Germany.
*E-mail address:* francesco.ciucci@uni-bayreuth.de (F. Ciucci).

[1] The experimental state, $\boldsymbol{\psi}$, is encoded in a vector. For example, for a battery experiment, the vector state could comprise the state of charge (SoC) and cycle number ($n$), implying $\boldsymbol{\psi} = \begin{pmatrix}\mathrm{SoC} & n\end{pmatrix}^\top$. While the theory in this article is developed with dependence on an experimental state vector, for the sake of clarity and without loss of generality, the DRT inversion from both synthetic and real experimental data is shown with respect to $\psi$, a scalar experimental state.

https://doi.org/10.1016/j.jpowsour.2024.235236
Received 1 July 2024; Received in revised form 31 July 2024; Accepted 12 August 2024
Available online 26 August 2024
0378-7753/

where $L_0(\boldsymbol{\psi})$, $R_\infty(\boldsymbol{\psi})$, and $\gamma(\log\tau,\boldsymbol{\psi})$ are the inductance, resistance, and the DRT, respectively. It should be noted that, to account for the dependence on the experimental state, we have encoded the $L_0(\boldsymbol{\psi})$, $R_\infty(\boldsymbol{\psi})$, and $\gamma(\log\tau,\boldsymbol{\psi})$ as functions parameterized on the experimental state ($\boldsymbol{\psi}$). In particular, $\gamma(\log\tau,\boldsymbol{\psi})$ is explicitly written as dependent on the log-timescale ($\log\tau$) with a parameterization on $\boldsymbol{\psi}$. This is consistent with our previous articles [22,36–38], where the DRT problem does not change relative to its formulation [37,38], but rather, the parametrization is shown explicitly.

Deconvolving $\gamma(\log\tau,\boldsymbol{\psi})$ from EIS data is challenging, as it requires solving an ill-posed inverse problem [39,40]. Regularized regression [41–46], deep neural networks [37], and other methods [33,34,47–54] have been developed for this purpose. Our group introduced a probabilistic approach for DRT deconvolution, reformulating regularized regression in a Bayesian context [55], including the Gaussian-process-based DRT (GP-DRT) model [56]. However, the GP-DRT method can produce negative DRT values (if a non-negativity constraint is not imposed through some inducing points) and is limited to the imaginary part of the EIS spectrum. To address these challenges, we developed the finite GP-DRT (fGP-DRT) framework [36], which inherits the key properties of GP-DRT, utilizes both components of the impedance, and enforces a non-negativity constraint on the DRT. While promising, the current fGP-DRT's limitation in deconvolving one EIS spectrum at a time restricts the analysis to a single experimental state without considering how several EIS spectra are correlated. This limitation could hinder the identification of electrochemical processes that evolve across conditions, such as oxygen partial pressure or temperature in fuel cells or cycle number, state of charge, or health in batteries.

This article addresses this limitation by extending the fGP model to explicitly incorporate dependence on the experimental state, $\boldsymbol{\psi}$. Specifically, $\gamma(\log\tau,\boldsymbol{\psi})$ is modeled as a GP with respect to $\boldsymbol{\psi}$ and a finite GP (fGP) with respect to $\log\tau$. Additionally, both $L_0(\boldsymbol{\psi})$ and $R_\infty(\boldsymbol{\psi})$ are assumed to be GPs. This framework is termed quasi-GP DRT (qGP-DRT) as it combines a GP (with respect to $\boldsymbol{\psi}$) with a fGP (with respect to $\log\tau$). This advancement allows for the simultaneous analysis of multiple EIS spectra (Fig. 1), providing a unified probabilistic DRT inversion framework across experimental conditions. To ensure its consistency, the qGP-DRT model was tested against noise-corrupted EIS synthetic experiments, showing that the deconvolved DRT closely matched analytical results. Furthermore, validation against real experimental data from fuel cells and batteries showed consistent DRT inversion against equivalent circuit models. Importantly, the qGP-DRT framework provides Bayesian probabilistic credible bands of impedance and DRT, allowing the assessment of the uncertainty with respect to both. In short, this work introduces a novel probabilistic approach for EIS data analysis based on Gaussian processes, paving the way for new research avenues in DRT analysis of multiple EIS spectra at a time.

## 2. Methods

As outlined in the Introduction, the qGP-DRT framework enhances the fGP-DRT model to handle multiple impedance spectra, allowing multidimensional experimental-dependent DRT inversion. This section covers its theoretical background, sampling process, and scoring used to check the consistency of the qGP-DRT model.

### 2.1. Theory

The qGP-DRT model assumes that $\gamma(\log\tau,\boldsymbol{\psi})$ is a zero-mean GP with respect to the experimental state vector, $\boldsymbol{\psi}$, and a fGP with respect to $\log\tau$ [36].[2] Additionally, the model approximates $\gamma(\log\tau,\boldsymbol{\psi})$ as

$$\gamma(\log\tau,\boldsymbol{\psi})\approx\sum_{n=1}^{N}\gamma(\log\tau_n,\boldsymbol{\psi})\,\phi_n(\log\tau) \tag{2}$$

where $\phi_n(\log\tau)$ is a basis function [36], $\gamma(\log\tau_n,\boldsymbol{\psi})$ is the DRT at the nodal points $\log\tau_n$ and $N$ is the number of collocation point with $\log\boldsymbol{\tau}=(\log\tau_1,\log\tau_2,\ldots,\log\tau_N)^\top$.

To illustrate the approach developed, we consider first only EIS data from a pair of spectra at two experimental states, $\boldsymbol{\psi}_p$ and $\boldsymbol{\psi}_q$. We denote the corresponding data as $\boldsymbol{Z}_p$ and $\boldsymbol{Z}_q$, which are the vectors concatenating the real and imaginary components of $p^{\text{th}}$ and $q^{\text{th}}$ experiments, respectively [36]. The vectors of probed frequencies can be generically denoted as $\boldsymbol{f}_p=\left(f_{p,1},f_{p,2},\ldots,f_{p,M_p}\right)^\top$ and $\boldsymbol{f}_q=\left(f_{q,1},f_{q,2},\ldots,f_{q,M_q}\right)^\top$, where $M_p$ and $M_q$ are not necessarily identical positive integers.

We consider the DRT discretization outlined by equation (2), such that the discretization vector for the $p^{\text{th}}$ experiment is $\boldsymbol{x}_p=\left(L_0(\boldsymbol{\psi}_p),R_\infty(\boldsymbol{\psi}_p),\gamma(\log\boldsymbol{\tau},\boldsymbol{\psi}_p)^\top\right)^\top$. Then, we can rewrite (1) as [36]

$$\boldsymbol{Z}_p=\mathbf{A}_p\boldsymbol{x}_p+\boldsymbol{\varepsilon}_p \tag{3a}$$

$$\boldsymbol{Z}_q=\mathbf{A}_q\boldsymbol{x}_q+\boldsymbol{\varepsilon}_q \tag{3b}$$

where $\mathbf{A}_p$ and $\mathbf{A}_q$ are obtained by discretizing the real and imaginary parts of the DRT impedances using the real ($\mathbf{A}_{\text{re},p}$) and imaginary ($\mathbf{A}_{\text{im},p}$), and the real ($\mathbf{A}_{\text{re},q}$) and imaginary ($\mathbf{A}_{\text{im},q}$), component matrices, respectively, so that $\mathbf{A}_p$ is given by [36]

$$\mathbf{A}_p=\begin{pmatrix}\mathbf{0} & \mathbf{1} & \mathbf{A}_{\text{re},p}\\ 2\pi\boldsymbol{f}_p & \mathbf{0} & \mathbf{A}_{\text{im},p}\end{pmatrix} \tag{4}$$

and $\boldsymbol{\varepsilon}_p\sim\mathcal{N}\left(0,\sigma_n^2\mathbf{I}_M\right)$ where $\sigma_n$ is a scalar and $\mathbf{I}_M$ is $M\times M$ identity matrix. For the $q^{\text{th}}$ experiment, definitions are analogous.

Assuming, the resistance, $R_\infty(\boldsymbol{\psi})$, and inductance, $L_0(\boldsymbol{\psi})$, are zero-mean GPs, such that $R_\infty(\boldsymbol{\psi})\sim\mathcal{GP}(0,k_R(\boldsymbol{\psi},\boldsymbol{\psi}'))$ and $L_0(\boldsymbol{\psi})\sim\mathcal{GP}(0,k_L(\boldsymbol{\psi},\boldsymbol{\psi}'))$ with kernels $k_R(\boldsymbol{\psi},\boldsymbol{\psi}')$ and $k_L(\boldsymbol{\psi},\boldsymbol{\psi}')$, respectively.

It follows from (3) that

$$\begin{pmatrix}\boldsymbol{x}_p\\ \boldsymbol{x}_q\end{pmatrix}\sim\mathcal{N}(0,\boldsymbol{\Gamma}) \tag{5}$$

where the covariance matrix, $\boldsymbol{\Gamma}$, is defined as

$$\boldsymbol{\Gamma}=\begin{pmatrix}\boldsymbol{\Gamma}_{pp} & \boldsymbol{\Gamma}_{pq}\\ \boldsymbol{\Gamma}_{pq}^\top & \boldsymbol{\Gamma}_{qq}\end{pmatrix} \tag{6}$$

and diagonal and off-diagonal blocks ($\boldsymbol{\Gamma}_{pp}$ and $\boldsymbol{\Gamma}_{pq}$, respectively) are

$$\boldsymbol{\Gamma}_{pp}=\begin{bmatrix}k_R(\boldsymbol{\psi}_p,\boldsymbol{\psi}_p) & 0 & 0\\ 0 & k_L(\boldsymbol{\psi}_p,\boldsymbol{\psi}_p) & 0\\ 0 & 0 & \mathbf{K}_{pp}\end{bmatrix} \tag{7a}$$

$$\boldsymbol{\Gamma}_{pq}=\begin{bmatrix}k_R(\boldsymbol{\psi}_p,\boldsymbol{\psi}_q) & 0 & 0\\ 0 & k_L(\boldsymbol{\psi}_p,\boldsymbol{\psi}_q) & 0\\ 0 & 0 & \mathbf{K}_{pq}\end{bmatrix} \tag{7b}$$

We can explicitly write the diagonal and off-diagonal blocks as

$$\left(\mathbf{K}_{pp}\right)_{nm}=k_\gamma\left((\log\tau_n,\boldsymbol{\psi}_p),(\log\tau_m,\boldsymbol{\psi}_p)\right) \tag{8a}$$

$$\left(\mathbf{K}_{pq}\right)_{nm}=k_\gamma\left((\log\tau_n,\boldsymbol{\psi}_p),(\log\tau_m,\boldsymbol{\psi}_q)\right) \tag{8b}$$

where $n,m=1,2,\ldots,N$. We can now generalize to the case of $N_\psi$ experimental conditions so that $\boldsymbol{x}=\begin{pmatrix}\boldsymbol{x}_1\\ \boldsymbol{x}_2\\ \vdots\\ \boldsymbol{x}_{N_\psi}\end{pmatrix}$ and $\boldsymbol{Z}_{\text{exp}}=\begin{pmatrix}\boldsymbol{Z}_1\\ \boldsymbol{Z}_2\\ \vdots\\ \boldsymbol{Z}_{N_\psi}\end{pmatrix}$ are

[2] We may write loosely that $\gamma(\boldsymbol{\psi}|\log\tau)\sim\mathcal{GP}(0,k(\boldsymbol{\psi},\boldsymbol{\psi}'))$ with kernel $k(\boldsymbol{\psi},\boldsymbol{\psi}')$, where $\gamma(\boldsymbol{\psi}|\log\tau)$ indicates that $\log\tau$ is fixed.

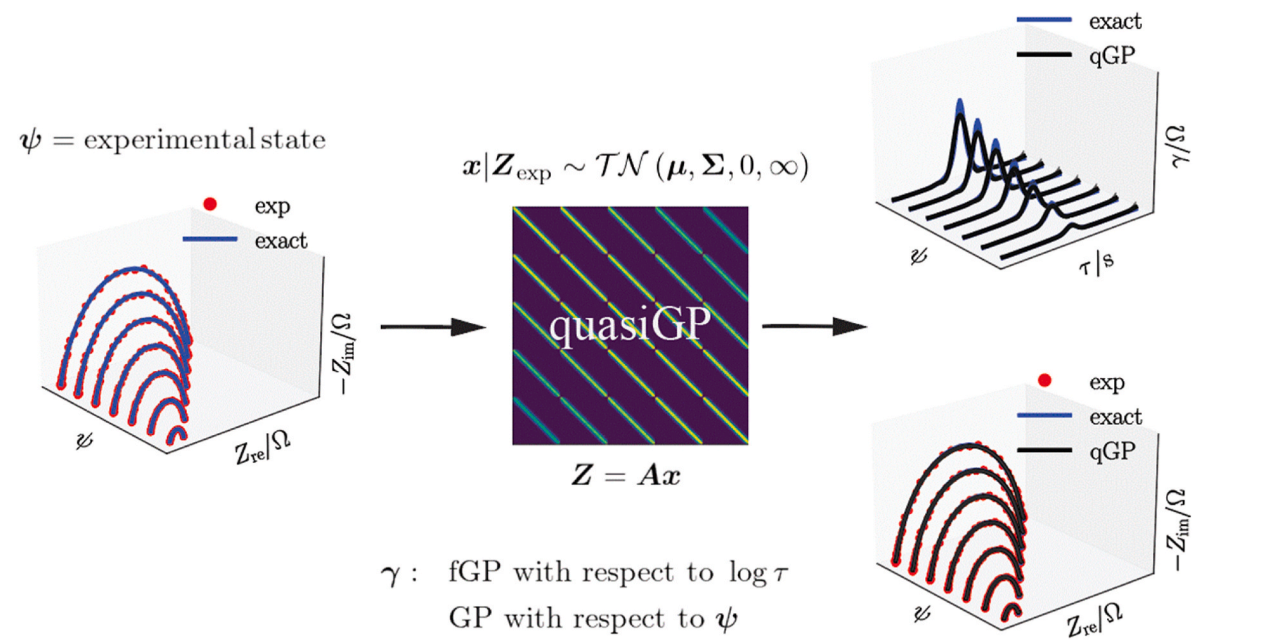


**Fig. 1.** Schematic illustration of the qGP-DRT framework.

the vectors of discretized DRTs and experimental impedances, respectively. Each vector $\boldsymbol{x}_k$ and $\boldsymbol{Z}_k$ (for $k = 1, 2, \ldots, N_\psi$ ) can be defined in an identical way as above. As in the fGP model [36], the distribution of $\boldsymbol{x}$ conditioned to the experimental data $\boldsymbol{Z}_{\rm exp}$ is a truncated multivariate normal such that [36,56]

$$\boldsymbol{x}|\boldsymbol{Z}_{\rm exp} \sim \mathscr{TN}(\boldsymbol{\mu}, \boldsymbol{\Sigma}, 0, \infty) \tag{9}$$

where the mean, $\boldsymbol{\mu}$, and covariance matrix, $\boldsymbol{\Sigma}$, are defined as

$$\boldsymbol{\mu} = \mathrm{abs}\left(\boldsymbol{\Gamma}\mathbf{A}^\top\left(\mathbf{A}\boldsymbol{\Gamma}\mathbf{A}^\top + \sigma_n^2\,\mathbf{I}_{N_\psi}\right)^{-1}\boldsymbol{Z}_{\rm exp}\right) \tag{10a}$$

$$\boldsymbol{\Sigma} = \boldsymbol{\Gamma} - \boldsymbol{\Gamma}\mathbf{A}^\top\left(\mathbf{A}\boldsymbol{\Gamma}\mathbf{A}^\top + \sigma_n^2\,\mathbf{I}_{N_\psi}\right)^{-1}\mathbf{A}\boldsymbol{\Gamma} \tag{10b}$$

and $\mathrm{abs}(\cdot)$ indicates elementwise absolute value, $\mathbf{I}_{N_\psi}$ is the $N_\psi \times N_\psi$ identity matrix, $\mathbf{A}$ is a block-diagonal matrix such that $\mathbf{A} = \mathrm{diag}(\mathbf{A}_1, \mathbf{A}_2, \ldots, \mathbf{A}_{N_\psi})$, and finally $\Gamma$ is generalized relative to (6) as

$$\boldsymbol{\Gamma} = \begin{pmatrix} \boldsymbol{\Gamma}_{11} & \boldsymbol{\Gamma}_{12} & \cdots & \boldsymbol{\Gamma}_{1N_\psi} \\ \boldsymbol{\Gamma}_{12}^\top & \boldsymbol{\Gamma}_{22} & \ddots & \boldsymbol{\Gamma}_{2N_\psi} \\ \vdots & \vdots & & \vdots \\ \boldsymbol{\Gamma}_{1N_\psi}^\top & \boldsymbol{\Gamma}_{2N_\psi}^\top & & \boldsymbol{\Gamma}_{N_\psi N_\psi} \end{pmatrix} \tag{11}$$

where the definition of each block is analogous to the block definition given in (6).

#### 2.1.1. Kernels

To compute the kernel blocks in (11) using (7) and (8), we employ the following kernels [36,56]:

$$k_\gamma((\log\tau, \boldsymbol{\psi}), (\log\tau', \boldsymbol{\psi}')) = \sigma_\nu^2\,\exp\left(-\frac{(\log\tau - \log\tau')^2}{2\ell_f^2}\right)\left(-\frac{\|\boldsymbol{\psi} - \boldsymbol{\psi}'\|_2^2}{2\ell_\psi^2}\right) \tag{12a}$$

$$k_R(\boldsymbol{\psi}, \boldsymbol{\psi}') = \sigma_R^2\,\exp\left(-\frac{\|\boldsymbol{\psi} - \boldsymbol{\psi}'\|_2^2}{2\ell_R^2}\right) \tag{12b}$$

$$k_L(\boldsymbol{\psi}, \boldsymbol{\psi}') = \sigma_L^2\,\exp\left(-\frac{\|\boldsymbol{\psi} - \boldsymbol{\psi}'\|_2^2}{2\ell_L^2}\right) \tag{12c}$$

where, $\sigma_\nu^2$, $\sigma_R^2$, $\sigma_L^2$, are the kernel's prefactors, $\ell_f$ , $\ell_R$, $\ell_L$, $\ell_\psi$ denote length scales, and $\|\cdot\|_2$ is the Euclidean norm.

#### 2.1.2. Hyperparameter optimization

Unless explicitly stated, the hyperparameter vector $\boldsymbol{\theta} = (\sigma_n, \sigma_\nu, \sigma_R, \sigma_L, \ell_f, \ell_\psi, \ell_R, \ell_L)^\top$ was obtained by maximizing the unbounded evidence, i.e., $p(\boldsymbol{Z}_{\rm exp}|\boldsymbol{\theta})$, which is given by

$$\log(p(\boldsymbol{Z}_{\rm exp}|\boldsymbol{\theta})) = \frac{1}{2}\,\boldsymbol{Z}_{\rm exp}^\top\left(\mathbf{A}\boldsymbol{\Gamma}\mathbf{A}^\top + \sigma_n^2\mathbf{I}_{N_\psi}\right)^{-1}\boldsymbol{Z}_{\rm exp} - \frac{1}{2}\log\left(\left|\mathbf{A}\boldsymbol{\Gamma}\mathbf{A}^\top + \sigma_n^2\mathbf{I}_{N_\psi}\right|\right) - \frac{(M_{\rm tot}+2)}{2}\log(2\pi) \tag{13}$$

where $M_{\rm tot} = \sum_{k=1}^{N_{\rm exp}} M_k$with $M_k$ being the number of frequencies probed during the $k^{\rm th}$ experiment.

As calculating the direct inverse and determinant of the large matrix in (13) can be numerically challenging, $\mathbf{A}\boldsymbol{\Gamma}\mathbf{A}^\top$ was approximated using a truncated singular value decomposition, such that $\mathbf{A}\boldsymbol{\Gamma}\mathbf{A}^\top \approx \mathbf{U}_r\mathbf{S}_r\mathbf{V}_r^\top$, where matrices $\mathbf{U}_r$ and $\mathbf{V}_r$ contain the first $r$ columns and rows of the orthogonal matrices $\mathbf{U}$ and $\mathbf{V}$, respectively, and $\mathbf{S}_r = \mathrm{diag}(\sigma_1, \sigma_2, \ldots, \sigma_r)$ contains the $r$ largest singular values of $\mathbf{A}\boldsymbol{\Gamma}\mathbf{A}^\top$ with $\sigma_1 > \sigma_2 > \ldots, \sigma_r$ (panel (a) of Fig. S1). Then, $\left(\mathbf{A}\boldsymbol{\Gamma}\mathbf{A}^\top + \sigma_n^2\mathbf{I}\right)^{-1}$ was approximated using the Sherman-Morrison-Woodbury's formula [57] as

$$\left(\mathbf{A}\boldsymbol{\Gamma}\mathbf{A}^\top + \sigma_n^2\mathbf{I}\right)^{-1} \approx \frac{1}{\sigma_n^2}\mathbf{I} - \frac{1}{\sigma_n^4}\mathbf{U}_r\left(\mathrm{diag}\left(\frac{\sigma_1\sigma_n^2}{\sigma_1+\sigma_n^2}, \frac{\sigma_2\sigma_n^2}{\sigma_2+\sigma_n^2}, \ldots, \frac{\sigma_r\sigma_n^2}{\sigma_r+\sigma_n^2}\right)\right)\mathbf{V}_r^\top \tag{14}$$

and the determinant $\left|\mathbf{A}\boldsymbol{\Gamma}\mathbf{A}^\top + \sigma_n^2\mathbf{I}\right|$ was approximated using the matrix inversion lemma [58] as

$$\left|\mathbf{A}\boldsymbol{\Gamma}\mathbf{A}^\top + \sigma_n^2\mathbf{I}\right| \approx \prod_{k=1}^{n}\left(\sigma_n^2 + \sigma_k\right) \tag{15}$$

*2.1.3. Sampling*

Relative to the previously used Hamiltonian Monte Carlo sampler [36], we added an adaptive step size [59] to sample $\boldsymbol{x}$ from (9). The adaptive step size optimizes exploration in Hamiltonian dynamics by monitoring acceptance rates: small steps slow sampling, and large steps introduce inaccuracy. The algorithm adjusts step size to balance efficiency (high acceptance) and exploration (finding diverse states). The step size dynamically adjusts based on the acceptance rate over 50-sample intervals. Rates below 90 % trigger a step-size decrease for more careful exploration, while rates above 90 % lead to an increase of the step size for faster exploration. This ensures efficient sampling within the desired constraints.

During sampling, 10,000 samples were generated with the initial 1000 samples being discarded as burn-in. Next, having generated 9000 samples of $\boldsymbol{x}$, the corresponding impedances, $\boldsymbol{Z}$, were obtained as $\boldsymbol{Z} = \mathbf{A}\boldsymbol{x}$. The 1st to 99th percentile credible intervals around the means were visualized as gray regions in corresponding plots.

### 2.2. Scoring the quality of the DRT and EIS recovery

To evaluate the quality of DRT and impedance recoveries, the following normalized mean square errors were used:

$$\mathrm{MSE}_{\mathrm{norm},\gamma} = \frac{1}{N_\psi}\sum_{k=1}^{N_\psi}\mathbb{E}\left(\frac{\left\|\boldsymbol{\gamma}_{\mathrm{exact},k} - \boldsymbol{\gamma}_k\right\|^2}{\left\|\boldsymbol{\gamma}_{\mathrm{exact},k}\right\|^2}\right) \tag{16a}$$

$$\mathrm{MSE}_{\mathrm{norm},Z} = \frac{1}{N_\psi}\sum_{k=1}^{N_\psi}\mathbb{E}\left(\frac{\left\|\boldsymbol{Z}_{\mathrm{exact},k} - \boldsymbol{Z}_k\right\|^2}{\left\|\boldsymbol{Z}_{\mathrm{exact},k}\right\|^2}\right) \tag{16b}$$

where $\mathbb{E}[.]$ denotes expected value computed from the samples obtained as described in the previous section, $\boldsymbol{\gamma}_{\mathrm{exact},k}$, is the exact DRT vector corresponding to exact impedance vector $\boldsymbol{Z}_{\mathrm{exact},k}$, $\boldsymbol{\gamma}_k$ and $\boldsymbol{Z}_{\mathrm{exact},k}$ are the correspondingly recovered DRT and impedance vectors, respectively. As above, $\boldsymbol{\gamma}$ is discretized with respect to $\log \boldsymbol{\tau}$.

### 2.3. Artificial experiment generation

The noise-corrupted artificial data were generated in the $10^{-2} - 10^6$ Hz frequency range with 10 points per decade by adding noise to the exact impedance $\boldsymbol{Z}_{\mathrm{exact}}$. Unless explicitly stated, the error standard deviation was set to $\sigma_n^{\mathrm{exp}} = 0.5\ \Omega$ .[3]

## 3. Results

Synthetic experiments were first used to validate the consistency and robustness of the qGP-DRT model. Then, the model was tested against real data from a fuel cell and battery under diverse experimental conditions.

### 3.1. Artificial experiments

We first considered EIS data originating from single ZARC, Havriliak-Negami, 2 × ZARC, Gerischer, and piecewise constant models [36,56,60] (their analytical expressions are reported elsewhere [41]). Without loss of generality, the experimental state is taken to be $\psi$, a scalar.

*3.1.1. Single ZARC and Havriliak-Negami models*

We initially investigated a single ZARC model consisting of an ohmic resistor ($R_\infty$) in series with a parallel circuit containing a resistor ($R_{\mathrm{ct}}$) and a constant phase element (CPE) [37]. Six synthetic experiments were generated with $R_{\mathrm{ct}}\ (\psi)$ exhibiting a dependence on $\psi$. Fig. 2 depicts the median DRTs and impedances ((panels (a) and (c)) recovered with the qGP-DRT model for $\psi = 0.0, 0.2, .., 1.0$). All DRTs and impedances (panels (a), (c) & (e)) were recovered accurately, as evidenced by the low $\mathrm{MSE}_{\mathrm{norm},\gamma} = 1.73 \times 10^{-2}$ and $\mathrm{MSE}_{\mathrm{norm},z} = 9.89 \times 10^{-6}$ values (Table S7). DRT peaks were consistently identified for all experimental conditions, with a noticeable peak decrease as $\psi$ increased (Fig. 2 (e)). The recovered qGP-DRT impedances closely matched the corresponding exact impedances (panel (a) of Fig. 2). To evaluate the computational scaling of the qGP-DRT framework, we generated 5 synthetic experiments with each $N_\psi = 10, 20, 30,$ and 40, and recorded the computational time.[4] We noted the scalability of the qGP-DRT model, given that 20 experiments took approximately 17 min (Figure S1 (b)).

We then investigated a scenario where $\tau_0\ (\psi)$ exhibited a dependence on $\psi$. Eleven EIS spectra were subsequently generated for $\psi = 0.0, 0.2, \ldots 1.0$. Panels (a), (b), and (c) of Fig. 3 show the magnitudes, qGP DRTs, and 2D qGP-DRT plots, respectively. Notably, the recovered qGP DRTs demonstrated characteristic response shifts as $\psi$ varied (panels (c) and (d) of Fig. 3). Furthermore, we applied the qGP-DRT model to analyze multiple EIS spectra derived from the Havriliak-Negami model. As for the single ZARC case, the DRTs and impedances were well recovered (see panels (b), (d), and (f) of Fig. 2).

*3.1.1.1. Influence of the experimental noise.* We evaluated the influence of experimental noise on the qGP-DRT framework. We employed a single ZARC model and generated synthetic experiments for various noise levels ($\sigma_n^{\mathrm{exp}} = 1$, 1.5, and 2.0 Ω) and $\psi = 0.0, 0.2, .., 1.0$). As above, we obtained hyperparameters optimally by maximizing the evidence at each noise level. The recovered qGP-DRTs and EIS are presented in Figs. S2 and S3. Even at elevated noise levels (1.5Ω and 2.0 Ω), the recovered DRTs and impedances closely matched their corresponding exact values (see Fig. S3).

Additionally, we considered frequency-dependent noise models defined elsewhere [41], with the artificial EIS data being generated at noise level $\sigma_n^{\mathrm{exp}} = 0.02\Omega$. Consistent with previous findings, the qGP DRTs and impedances closely matched the corresponding exact and experimental impedances (Fig. S4), as confirmed by the low values of $\mathrm{MSE}_{\mathrm{norm},\gamma}$ and $\mathrm{MSE}_{\mathrm{norm},Z}$ for all $\sigma_n^{\mathrm{exp}}$ listed in Table S7.

*3.1.2. Multiple ZARCs*

We first studied the 2 × ZARC model, which consists of two ZARCs (Section 2.1.1) in series. These circuits were chosen to exhibit overlapping, separated, or distant timescales (see the circuit parameters in Tables S2 and S3). Six synthetic EIS spectra were generated with $R_{\mathrm{ct},2}(\psi)$ and $\tau_2\ (\psi)$ exhibiting a dependence on $\psi$.

For the case of the separated 2 × ZARC ($\tau_1 = 1.0 \times 10^{-1}$s, $\tau_2 = 1.0 \times 10^{-3}$ s), the Nyquist plots and the qGP DRTs are presented in panels (a) and (c) of Fig. S5, respectively. Consistent with our observations for the single ZARC model (Section 2.1.1), the qGP-DRT model successfully identified the DRT peaks and recovered the impedances across all experimental conditions. As shown in panels (c) and (e) of Fig. S5, the qGP DRTs exhibited two distinct peaks: one prominent for all $\psi$, and a second peak that diminishes with changing $\psi$. The overlapping 2 × ZARC model (with $\tau_1 = 1.0\times 10^{-1}$s, $\tau_2 = 1.0\times 10^{-2}$s) was also well recovered, as demonstrated in panels (b) and (d) of Fig. S5.

These findings were further confirmed for the distant 2 × ZARC and 3 × ZARC models with the estimated median DRTs and impedances closely matching their corresponding exact values (see Figs. 4 and 5). Additionally, the low $\mathrm{MSE}_{\mathrm{norm},\gamma}$ and $\mathrm{MSE}_{\mathrm{norm},z}$ values in Table S7 corroborated the quality of the DRT and impedance recovery by the qGP-DRT model.

[3] $\sigma_n^{\mathrm{exp}}$ is the standard deviation of the noise in the artificial experiments analogous to $\boldsymbol{\varepsilon} \sim \mathcal{N}\left(0, \sigma_n^{\mathrm{exp}}\mathbf{I}\right)$ in equation (3). Instead, $\sigma_n$ is one of the hyperparameters of the qGP-DRT model originating from equation (3).

[4] The clock time was measured using an Intel(R) Core (TM) i5-10300H CPU with a 2.50 GHz clock rate in a laptop computer equipped with 16 GB of RAM.

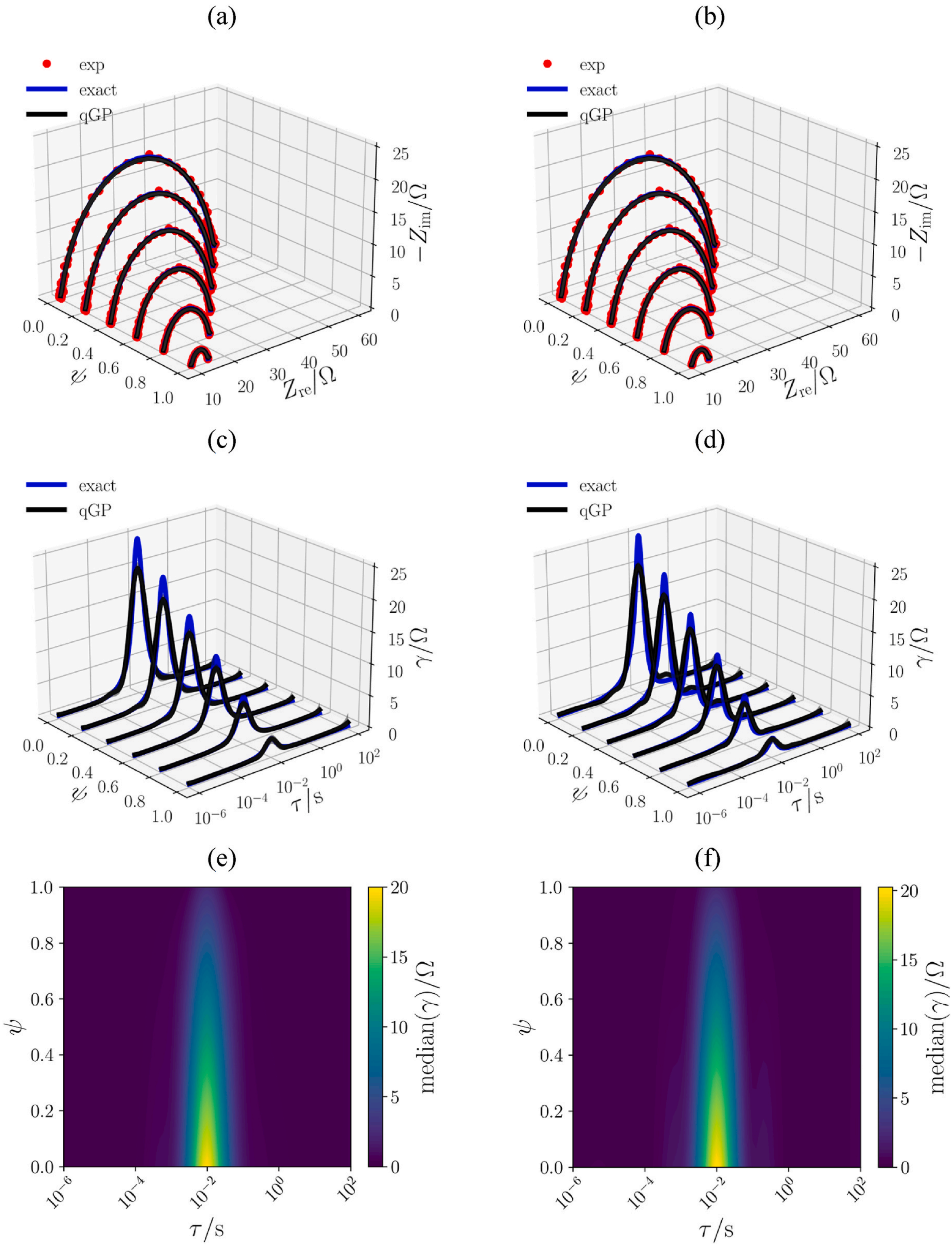


**Fig. 2.** Nyquist plots of the single ZARC (a) and Havriliak-Negami models (b) with $R_{\mathrm{ct}}(\psi)$ exhibiting a dependence on $\psi$ ($\sigma_n^{\mathrm{exp}} = 0.5\Omega$). Panels (c) and (d) show the corresponding recovered qGP DRTs, with associated 2D contour plots of median DRTs in panels (e) and (f).

#### 3.1.3. Discontinuous DRT

We extended the analysis to two discontinuous models, namely the Gerischer and piecewise constant models, whose circuit's parameters values are provided in Table S4. The corresponding recovered qGP DRTs and impedances are presented in Fig. S6. We observed that the qGP-DRT model approximately captured discontinuities.

### 3.2. Real experiments

Having established that the qGP-DRT model is consistent against well-controlled, analytical models, we evaluated its effectiveness in handling real-world data leveraging EIS spectra from a fuel cell and battery.

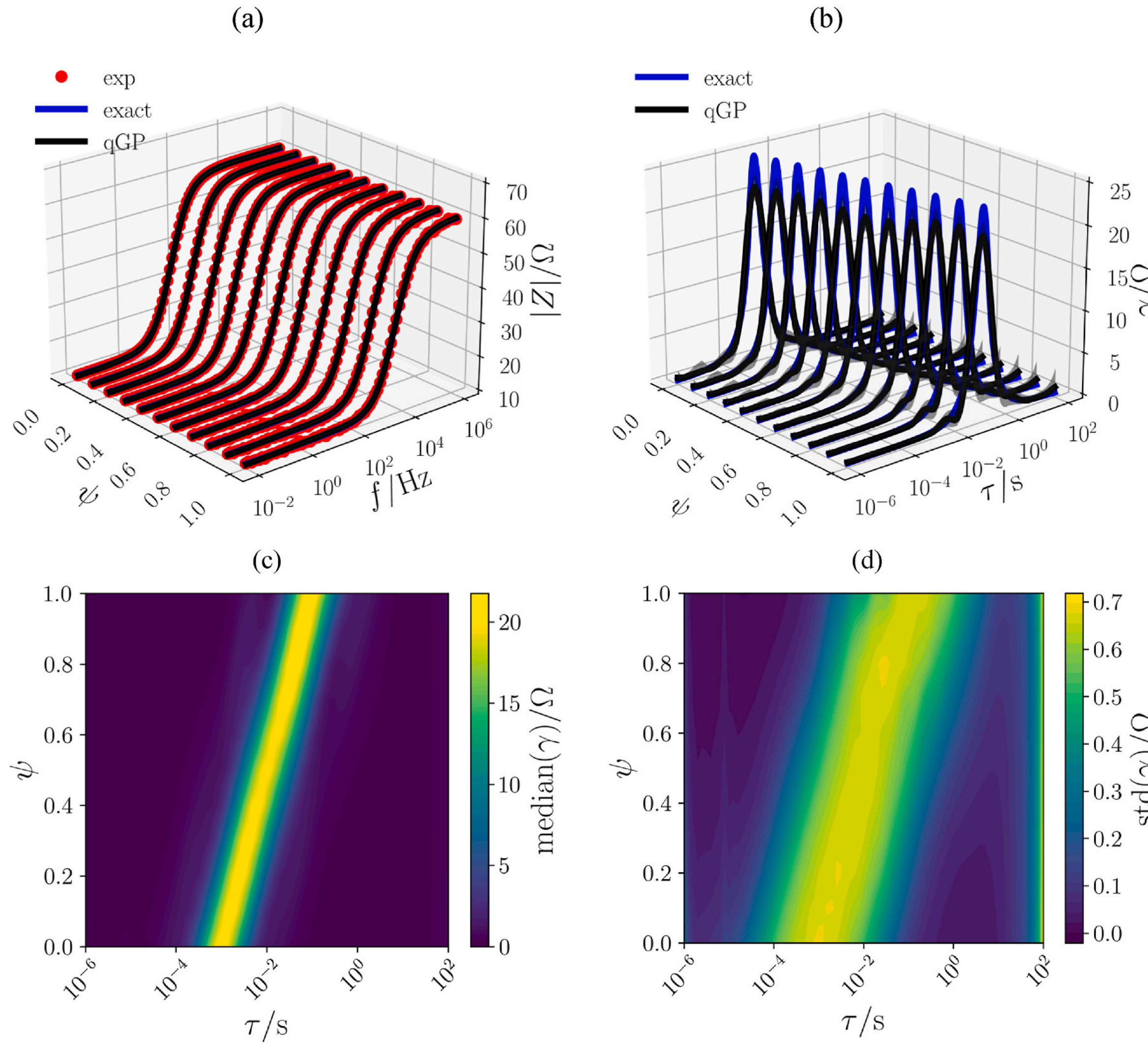


**Fig. 3.** (a) Magnitudes for the single ZARC model with $\tau_0(\psi)$ exhibiting dependence on $\psi$ ($\sigma_n^{\rm exp} = 0.5\Omega$). Panel (b) shows corresponding qGP DRTs, while panels (c) and (d) display 2D contour plots of the median and standard deviation, respectively.

### 3.2.1. *Symmetric protonic ceramic fuel cell*

We analyzed data from a symmetric cell featuring $Ba_{0.95}La_{0.05}FeO_{3\text{-}\delta}$ (BLF) as the electrode materials and a samarium-doped ceria as the electrolyte. The cell was operated at 550 °C in an $N_2/O_2$ atmosphere under varying oxygen partial pressures ($pO_2$ = 21, 40, 60, 80, and 100 %). EIS data were collected across the frequency range 100 mHz to 20 kHz with five points recorded per decade. The data were regressed using 2 × ZARC ECM, with the parameters provided in Table S5. The qGP-DRT model successfully identified the DRT peaks for all experimental conditions, as shown in Fig. 6 (panels (c) and (e)). Additionally, the qGP-DRT model matched with the DRTtools,[5] the fitted ECM and the experimental data (panel (a) and (c) Fig. 6), as evidenced by the low $\text{MSE}_{\text{norm},\gamma}$ and $\text{MSE}_{\text{norm},Z}$ values in Table S8.

### 3.2.2. *Lithium-metal battery*

Next, we investigated a lithium-ion battery with a $LiFePO_4$ (LFP) cathode, a lithium-metal anode, and 1M $LiPF_6$ in ethylene carbonate: diethyl carbonate (1:1 v/v) as an electrolyte [62]. EIS measurements were collected at frequencies ranging from 0.1 Hz to 7 MHz with a 5C charge-discharge rate at cycles 30, 60, 90, and 120. The data were regressed using a 2 × ZARC ECM, with the parameters provided in Table S6.

The qGP-DRT model successfully recovered the DRTs and impedances, the corresponding DRTs were in good agreement with DRTtools and ECM results (Fig. 6, panels (b) and (d)). Well-defined peaks were consistently identified $\tau = 10^{-4}$ s for all experimental conditions (Fig. 6 (f)). Furthermore, the low $\text{MSE}_{\text{norm},\gamma}$ and $\text{MSE}_{\text{norm},Z}$ values in Table S8 confirmed the effectiveness of the qGP-DRT regression. Additionally, the narrow credible bands in Fig. 6 (d) indicated low uncertainty and high confidence in the recovered DRTs.

## 4. Remarks and future directions

The qGP-DRT framework developed in this work enables simultaneous probabilistic analysis of multiple EIS spectra. We validated its effectiveness and consistency against both artificial and real datasets, with model hyperparameters optimally selected through evidence maximization. Despite its promise, several avenues for future improvements can be identified.

To enhance computational efficiency in EIS data analysis, we employed singular value decomposition for low-rank matrix approximation and adaptive step-size HMC sampling. However, challenges

[5] For the pyDRTtools settings, Gaussian radial basis functions for the discretization, and the full impedance spectrum were used. A regularization second-order derivative matrix was employed, and the regularization parameter was computed using the generalized cross-validation [41,61].

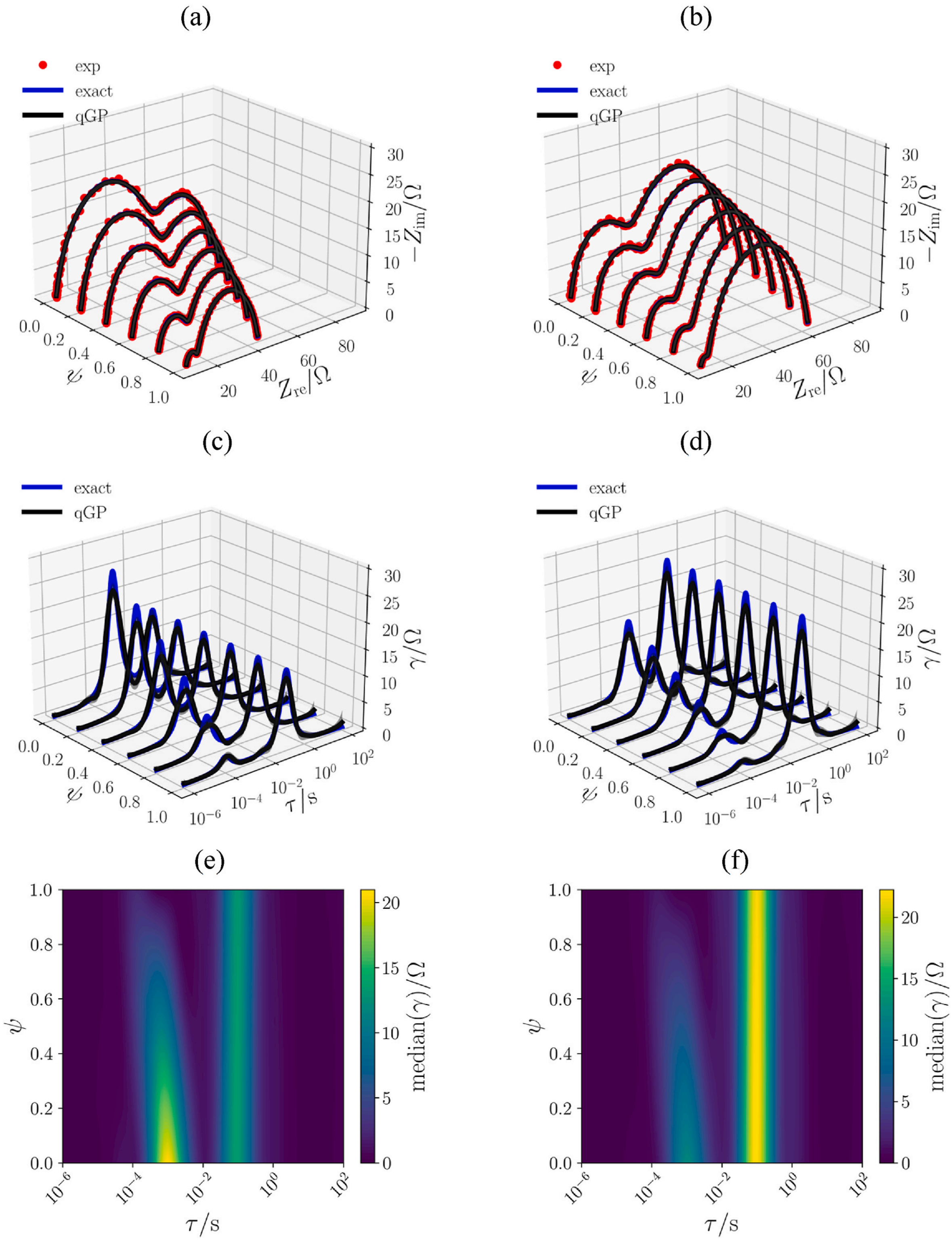


**Fig. 4.** Nyquist plots of the distant 2 × ZARC model for two conditions: (a) $R_{\rm ct,1} < R_{\rm ct,2}$ and (b) $R_{\rm ct,1} > R_{\rm ct,2}$. In both conditions, $R_{\rm ct,2}$ ($\psi$) and $\tau_2(\psi)$ exhibit a dependence on $\psi$ ($\sigma_n^{\rm exp} = 0.5\Omega$, $\tau_1 = 1.0 \times 10^{-1}$ s , and $\tau_2 = 1.0 \times 10^{-3}$ s). Panels (c) and (d) depict the corresponding recovered qGP DRTs, along with their associated 2D contour plots of median DRTs in panels (e) and (f).

remain in handling large-scale datasets efficiently. Future research should explore alternative low-rank approximation techniques beyond SVD to further optimize computational speed and accuracy [63]. Additionally, investigating advanced sampling approaches that enable direct sampling from high-dimensional spaces could potentially accelerate the analysis process [59]. Finally, the integration of scalable GP approximations such as sparse GPs and distributed GPs, could improve scalability and performance for large-scale or distributed EIS data analysis [36]. These advancements could collectively lead to faster analysis time, greater accuracy, and the ability to handle larger EIS datasets more effectively.

In our current work, we employed evidence maximization for

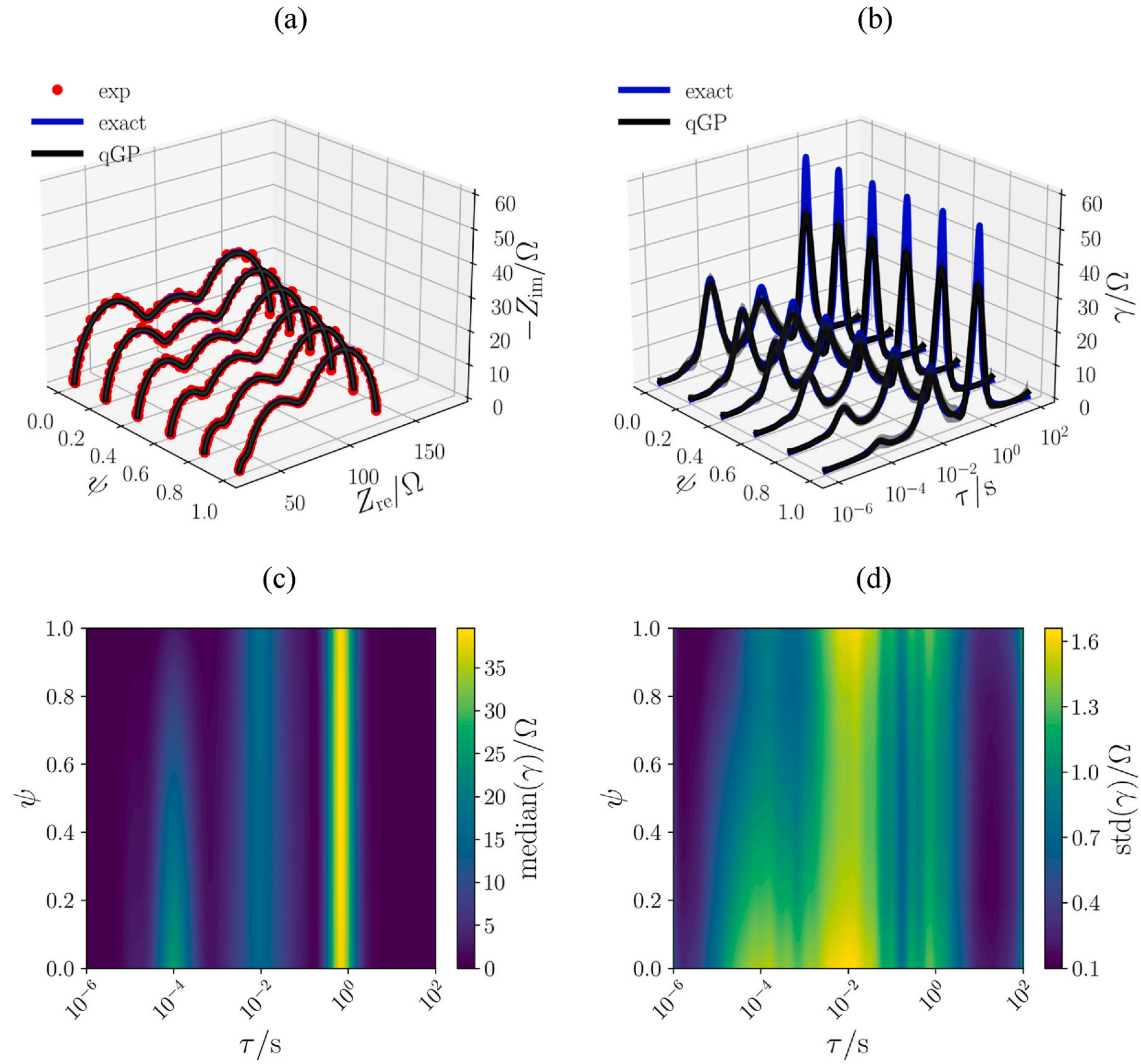


**Fig. 5.** (a) Nyquist plots of the distant 3 × ZARC model with $R_{\rm ct,1}$ ($\psi$) exhibiting a dependence on $\psi$ ($\sigma_n^{\rm exp} = 0.5\Omega$, $\tau_1 = 1.0 \times 10^{-4}$ s, $\tau_2 = 1.0 \times 10^{-2}$ s, and $\tau_3 = 1.0 \times 10^{-1}$ s). Panel (b) shows the corresponding qGP DRTs, while panels (c) and (d) display 2D contour plots of the median and standard deviation, respectively.

hyperparameter selection [36,64]. However, exploring alternative approaches, such as using products of GP experts as surrogate models, could potentially address scalability challenges, though with a possible trade-off in predictive accuracy [65]. This remains a significant avenue for future research.

A key challenge in our current framework is accurately capturing discontinuities in the DRT, which are essential for representing elements like fractal, Gerischer, and piecewise constant impedance. The inherently smooth nature of GPs poses limitations in this regard. Future research should investigate integrating hierarchical GP methods, such as the deep GPs [66] or other Bayesian methods [55] to enhance the recovery of DRT discontinuities, thereby improving the framework's ability to model complex impedance behaviors and expanding its applicability in EIS data analysis.

## 5. Conclusions

This work introduces a novel qGP-DRT framework, enabling simultaneous deconvolution of the DRT from EIS data acquired under various experimental conditions. Inheriting key features from the previously developed fGP-DRT model, this approach maintains a probabilistic GP foundation, robustness to experimental noise, and, unlike the vanilla GP-DRT, full utilization of complete impedance spectra and non-negativity of the recovered DRTs. Notably, the qGP-DRT model simplifies to the fGP-DRT model when considering a single experimental condition. Unlike the fGP-DRT model, the qGP-DRT model can invert the DRT across multiple experimental conditions, effectively bridging dependencies on both frequencies and experimental states. Validation on synthetic and real EIS datasets confirms the consistency and effectiveness of the approach. In short, this article introduces a novel methodology for the probabilistic analysis of multiple EIS spectra, paving the way for further research using GP-based methods for DRT deconvolution.

## Code availability

Relevant code is available at https://github.com/ciuccislab/quasiGP.

## CRediT authorship contribution statement

**Adeleke Maradesa:** Writing – review & editing, Writing – original draft, Visualization, Validation, Software, Methodology, Investigation, Formal analysis, Data curation, Conceptualization. **Baptiste Py:** Writing

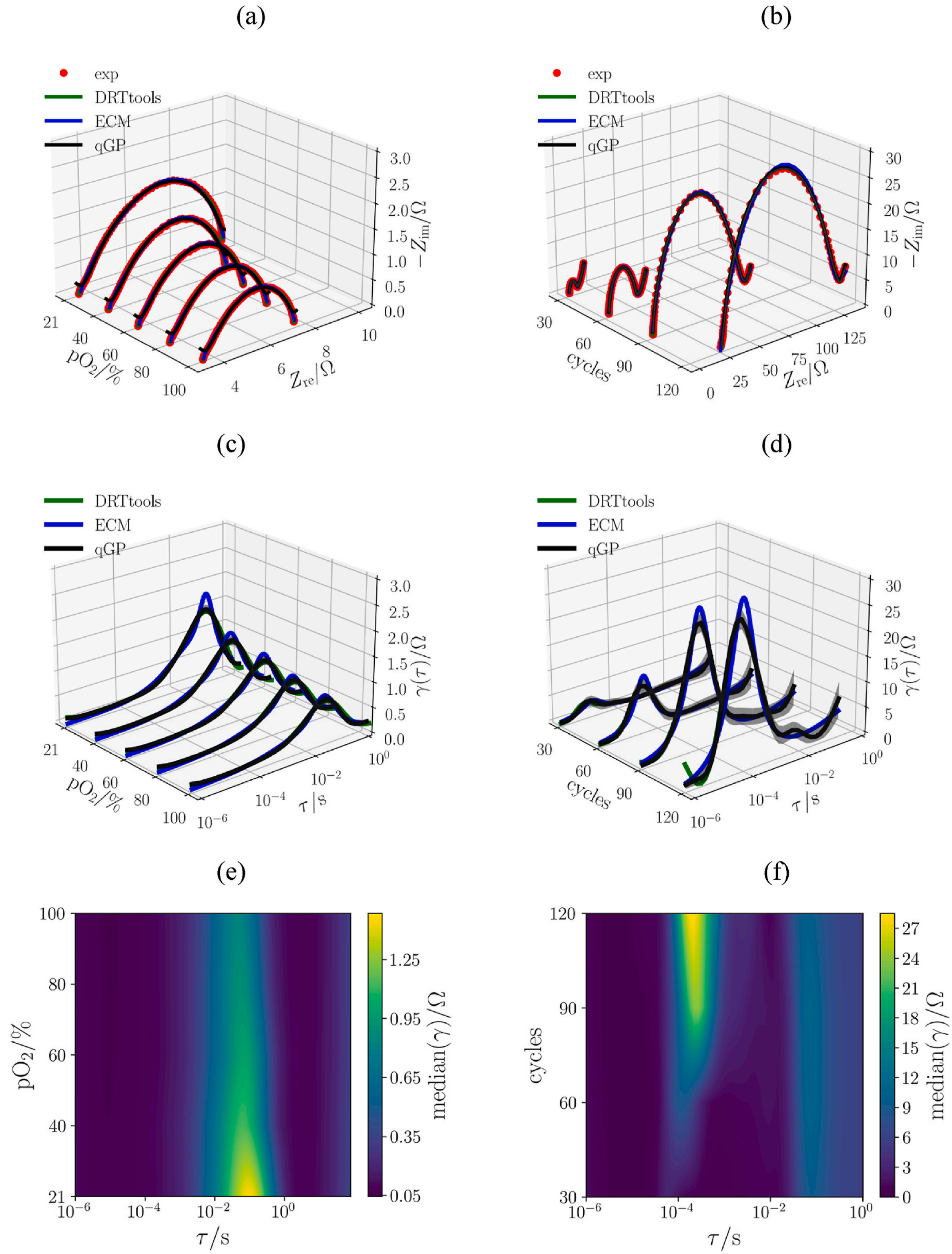


**Fig. 6.** Nyquist plots of the impedance from fuel cell with BLF (a) and LFP (b) electrodes. Panels (c) and (d) show the corresponding recovered qGP DRTs, along with their associated 2D contour plots for median DRTs in panels (e) and (f).

– review & editing, Methodology. **Francesco Ciucci:** Writing – review & editing, Visualization, Validation, Supervision, Software, Resources, Project administration, Methodology, Investigation, Funding acquisition, Conceptualization.

## Declaration of generative AI and AI-assisted technologies in the writing process

To enhance clarity and readability, Gemini Advanced was utilized to assist in the revision process. Following this, the manuscript underwent a comprehensive review and revision by the authors. Dr. Mark Ellwood further refined the language for clarity and grammatical accuracy. The authors assume full responsibility for the final content of the manuscript.

## Declaration of competing interest

No conflict of interest statement.

## Data availability

The companion code will be released on our GitHub channel upon paper acceptance

## Acknowledgments

The authors gratefully acknowledge the Research Grant Council of Hong Kong for support through the projects 18201820 and 16201622. A. Maradesa and B. Py also thank the Hong Kong PhD. Fellowship Scheme for its financial support. F. Ciucci also thanks the University of Bayreuth and the Bavarian Center for Battery Technology (BayBatt) for providing a start-up fund.

## Appendix A. Supplementary data

Supplementary data to this article can be found online at https://doi.org/10.1016/j.jpowsour.2024.235236.

## List of Symbols

*Greek letters*

| | |
|---|---|
| $\mathbf{\Gamma}$ | Covariance matrix for all sets of experiments |
| $\mathbf{\Gamma}_{pq}$ | Covariance matrix for $p^{\text{th}}$ and $q^{\text{th}}$ experiments |
| $\boldsymbol{\gamma}$ | DRT vector |
| $\gamma(\log\tau, \boldsymbol{\psi})$ | Distribution of relaxation times |
| $\boldsymbol{\gamma}_{\text{exact}}$ | Analytical DRT vector |
| $\boldsymbol{\varepsilon}$ | Vector of experimental errors |
| $\boldsymbol{\theta}$ | Vector of hyperparameters |
| $\boldsymbol{\mu}$ | Mean vector for the overall experiments |
| $\mathbf{\Sigma}$ | Covariance matrix for the overall experiments |
| $\sigma_L$ | Prefactor for the kernel $k_R(\boldsymbol{\psi}, \boldsymbol{\psi}')$ |
| $\sigma_n$ | GP hyperparameter |
| $\sigma_n^{\text{exp}}$ | Experimental error |
| $\sigma_R$ | Prefactor for the kernel $k_L(\boldsymbol{\psi}, \boldsymbol{\psi}')$ |
| $\sigma_r$ | Retained singular value |
| $\sigma_v$ | Prefactor for the kernel $k_\gamma((\log\tau, \boldsymbol{\psi}), (\log\tau', \boldsymbol{\psi}'))$ |
| $\tau$ | Relaxation time |
| $\phi_n(\log\tau)$ | Basis function |
| $\boldsymbol{\psi}$ | Vector of experimental conditions |

*Latin letters*

| | |
|---|---|
| $\mathbf{A}$ | Discretization matrix for the overall experiments |
| $\mathbf{A}_p$ | Discretization matrix for $p^{\text{th}}$ experiment |
| $\boldsymbol{f}$ | Frequency vector |
| $\mathbf{K}$ | Covariance matrix |
| $k$ | GP kernel |
| $L_0$ | Inductance |
| $\ell_f$ and $\ell_\psi$ | Length scales for the kernel $k_\gamma((\log\tau, \boldsymbol{\psi}), (\log\tau', \boldsymbol{\psi}'))$ |
| $\ell_L$ | Length scale for $k_L(\boldsymbol{\psi}, \boldsymbol{\psi}')$ |
| $\ell_R$ | Length scale for $k_R(\boldsymbol{\psi}, \boldsymbol{\psi}')$ |
| $M$ | Number of frequencies |
| $M_{\text{tot}}$ | Number of frequencies for all experiments |
| $\text{MSE}_{\text{norm},\gamma}$ | Normalized DRT mean square error |
| $\text{MSE}_{\text{norm},Z}$ | Normalized impedance mean square error |
| $N$ | Number of collocation points |
| $N_\psi$ | Number of experimental conditions |
| $R_{\text{ct}}$ | Charge-transfer resistance |
| $R_\infty$ | Ohmic resistance |
| $\mathbf{S}_r$ | The diagonal matrix containing all the singular values |
| $\mathbf{U}_r$ and $\mathbf{V}_r$ | The matrices containing the first $r$ columns and rows of the orthogonal matrices $\mathbf{U}$ and $\mathbf{V}$ |
| $\boldsymbol{x}$ | Vector of discretized DRTs for the overall experiment |
| $\boldsymbol{x}_p$ and $\boldsymbol{x}_q$ | Vector of discretized DRTs for $p$ and $q$ experiments |
| $\boldsymbol{Z}$ | Vector of the recovered impedance |
| $\boldsymbol{Z}_{\text{exact}}$ | Vector of analytical impedance |
| $\boldsymbol{Z}_{\text{exp}}$ | Vector of experimental impedance |
| $\boldsymbol{Z}_p$ and $\boldsymbol{Z}_q$ | Vector of experimental impedance for $p$ and $q$ experiments |

*List of Abbreviations*

| | |
|---|---|
| BLF | $Ba_{0.95}La_{0.05}FeO_{3-\delta}$ |
| fGP | finite Gaussian processes |
| DRT | Distribution of relaxation times |
| ECM | Equivalent circuit model |
| EIS | Electrochemical impedance spectroscopy |
| GPs | Gaussian processes |
| LFP | $LiFePO_4$ |
| $pO_2$ | Oxygen partial pressure |
| SoC | State of charge |
| SVD | Singular value decomposition |
| qGPs | quasi-GPs |
| std | Standard deviation |

## References


[1] V. Vivier, M.E. Orazem, Impedance analysis of electrochemical systems, Chem. Rev. 122 (2022) 11131–11168, https://doi.org/10.1021/acs.chemrev.1c00876.

[2] S. Wang, J. Zhang, O. Gharbi, V. Vivier, M. Gao, M.E. Orazem, Electrochemical impedance spectroscopy, Nat. Rev. Methods Primes 1 (2021) 41, https://doi.org/10.1038/s43586-021-00039-w.

[3] B. Yang, D. Wang, S. Chen, X. Sun, B. Yu, Electrochemical impedance preprocessing with distribution of relaxation time transform, J. Power Sources 571 (2023) 233062, https://doi.org/10.1016/j.jpowsour.2023.233062.

[4] M.E. Orazem, T. Tribollet, Electrochemical Impedance Spectroscopy, John Wiley & Sons, Inc, 2017.

[5] P. Niu, K. Yang, Z. Song, Z. Pang, Z. Feng, J. Meng, An efficient electrochemical optimizer for the distribution of relaxation times of lithium-ion batteries, J. Power Sources 605 (2024) 234489, https://doi.org/10.1016/j.jpowsour.2024.234489.

[6] Y. Lu, C.Z. Zhao, J.Q. Huang, Q. Zhang, The timescale identification decoupling complicated kinetic processes in lithium batteries, Joule 6 (2022) 1172–1198, https://doi.org/10.1016/j.joule.2022.05.005.

[7] A. Weber, Impedance analysis of porous electrode structures in batteries and fuel cells, TM - Tech. Mess. 88 (2020) 84, https://doi.org/10.1515/teme-2020-0084.

[8] J.P. Schmidt, P. Berg, M. Schonleber, A. weber, E. Ivers-Tiffée, The distribution of relaxation times as basis for generalized time-domain models for Li-ion batteries, J. Power Sources 221 (2013) 70–77, https://doi.org/10.1016/j.jpowsour.2012.07.100.

[9] L. Han, Y. Shang, Q. Liang, Y. Liu, Z. Guo, Distribution of relaxation times used for analyzing the electrochemical impedance spectroscopy of polymer electrolyte membrane fuel cell, Renew. Energy 227 (2024) 120485, https://doi.org/10.1016/j.renene.2024.120485.

[10] Y. Ao, Z. Li, S. Laghrouche, D. Depernet, D. Candusso, K. Zhao, Stack-level diagnosis of proton exchange membrane fuel cell by the distribution of relaxation times analysis of electrochemical impedance spectroscopy, J. Power Sources 603 (2024) 234420, https://doi.org/10.1016/j.jpowsour.2024.234420.

[11] E.H. Balaguera, J. Bisquert, Accelerating the assessment of hysteresis in perovskite solar cells, ACS Energy Lett. 9 (2024) 478–486, https://doi.org/10.1021/acsenergylett.3c02779.

[12] A. Omar, M.S. Ali, N. Abd Rahim, Electron transport properties analysis of titanium dioxide dye-sensitized solar cells ($TiO_2$-DSSCs) based natural dyes using electrochemical impedance spectroscopy concept: a review, Sol. Energy 207 (2020) 1088–1121, https://doi.org/10.1016/j.solener.2020.07.028.

[13] Y. Li, Y. Jiang, J. Dang, X. Deng, B. Liu, J. Ma, F. Yang, M. Ouyang, X. Shen, Application of distribution of relaxation times method in polymer electrolyte membrane water electrolyzer, J. Chem. Eng. 451 (2023) 138327, https://doi.org/10.1016/j.cej.2022.138327.

[14] G. Wang, A. Tricker, J.T. Lang, J. Wang, I. Zenyuk, D.-J. Liu, R. Mukundan, X. Peng, Understanding performance limitation of liquid alkaline water electrolyzers, J. Electrochem. Soc. 171 (2024) 06450, https://doi.org/10.1149/1945-7111/ad4fe6.

[15] A. Gado, R.J. Quimet, L. Bonville, S. Bliznakov, R. Maric, Analysis of electrochemical impedance spectroscopy using distribution of relaxation times for proton exchange membrane fuel cells and electrolyzers, Electrochem. Soc. Meet. Abstr. 240 (2021) 1261, https://doi.org/10.1149/MA2021-02411261mtgabs.

[16] R.G. Ramirez-Chavarria, E. Castillo-Villaneueva, B.E. Alvarez-Serna, L. Torres, R. M. Ramirez-Zamora, G. Buitron, L. Alvarez-Icaza, Automatic analysis of isothermal amplification via impedance time-constant-domain spectroscopy: a SARS-CoV-2 case study, Chemosensors 230 (2023) 2–13, https://doi.org/10.3390/chemosensors11040230.

[17] X. Huo, G. Shan, L. Yang, L. Gao, Y. Wang, M. Zhang, Y. Fu, W. Li, J. Zhang, Impedance analysis of alkaline water electrolysis based on distribution of relaxation time, Int. J. Hydrogen Energy 53 (2024) 684–697, https://doi.org/10.1016/j.ijhydene.2023.12.086.

[18] S.V. Pandey, N. Parikh, A. Mahapatra, A. Kalam, S. Akin, S. Satapathi, D. Prochowicz, P. Yadav, Deconvoluting the impedance response of halide perovskite single crystals: the distribution of relaxation time method, J. Phys. Chem. C 127 (2023) 11609–11615, https://doi.org/10.1021/acs.jpcc.3c01850.

[19] K. Krukiewicz, Electrochemical impedance spectroscopy as a versatile tool for the characterization of neural tissue: a mini review, Electrochem. Commun. 116 (2020) 106742, https://doi.org/10.1016/j.elecom.2020.106742.

[20] B.A. Boukamp, A. Rolle, Use of a distribution function of relaxation times (DFRT) in impedance analysis of SOFC electrodes, Solid State Ionics 314 (2018) 103–111, https://doi.org/10.1016/j.ssi.2017.11.021.

[21] M.V. Haeverbeke, B.D. Baets, M. Stock, Evaluating the potential of distribution of relaxation times analysis for plant agriculture, Comput. Electron. Agric. 213 (2023) 108249, https://doi.org/10.1016/j.compag.2023.108249.

[22] F. Ciucci, Modeling electrochemical impedance spectroscopy, Curr. Opin. Electrochem. 13 (2019) 132–139, https://doi.org/10.1016/j.coelec.2018.12.003.

[23] A. Maradesa, B. Py, J. Huang, Y. Lu, P. Iurilli, A. Mrozinski, et al., Advancing electrochemical impedance analysis through innovations in the distribution of relaxation times method, Joule 8 (2024) 1–24, https://doi.org/10.1016/j.joule.2024.05.008.

[24] A. Mrozinki, S. Molin, J. Karczewski, T. Miruszewski, P. Jasinki, Electrochemical properties of porous $Sr_{0.86}Ti_{0.65}Fe_{0.35}O_3$ oxygen electrodes in solid oxide cells: impedance study of symmetrical electrodes, Int. J. Hydrogen Energy 44 (2019) 1827–1838, https://doi.org/10.1016/j.ijhydene.2018.11.203.

[25] A.R.C. Bredar, A.L. Chown, A.R. Burton, B.H. Farnum, Electrochemical impedance spectroscopy of metal oxide electrodes for energy application, ACS Appl. Energy Mater. 3 (2020) 66–98, https://doi.org/10.1021/acsaem.9b01965.

[26] R. He, Y. He, W. Xie, B. Guo, S. Yang, Comparative analysis for commercial Li-ion batteries degradation using the distribution of relaxation time method based on electrochemical impedance spectroscopy, Energy 263 (2023) 125972, https://doi.org/10.1016/j.energy.2022.125972.

[27] P. Iurilli, B. Claudion, R.E. Carrillo, V. Wood, Physics-based SoH estimation for Li-ion cells, Batteries 8 (2022) 204, https://doi.org/10.3390/batteries8110204.

[28] Q. Zhang, D. Wang, E. Schaltz, D.I. Stroe, A. Gismero, B. Yang, Degradation mechanism analysis and State-of-Health estimation for lithium-ion batteries based on distribution of relaxation times, J. Energy Storage 55 (2022) 105386, https://doi.org/10.1016/j.est.2022.105386.

[29] L. Zhang, X. Hong, W. Xu, D. Ruan, Research on estimating the state of health of power batteries based on the distribution of relaxation times method, J. Power Sources 94 (2024) 112370, https://doi.org/10.1016/j.est.2024.112370.

[30] S. Liu, Q. Meyer, C. Jia, S. Wang, C. Rong, Y. Nie, C. Zhao, Operando deconvolution of the degradation mechanisms of iron–nitrogen–carbon catalysts in proton exchange membrane fuel cells, Energy Environ. Sci. 16 (2023) 3792, https://doi.org/10.1039/D3EE01166F.

[31] H. Dai, H. Kou, H. wang, L. Bi, Electrochemical performance of protonic ceramic fuel cells with stable $BaZrO_3$-based electrolyte: a mini-review, Electrochem. Commun. 96 (2018) 11–15, https://doi.org/10.1016/j.elecom.2018.09.001.

[32] M. Bruch, L. Millet, J. Kowal, M. Vetter, Novel method for the parameterization of a reliable equivalent circuit model for the precise simulation of a battery cell's electric behavior, J. Power Sources 490 (2021) 229513, https://doi.org/10.1016/j.jpowsour.2021.229513.

[33] S. Dierickx, A. Weber, E. Ivers-Tiffée, How the distribution of relaxation times enhances complex equivalent circuit models for fuel cells, Electrochim. Acta 355 (2020) 136764, https://doi.org/10.1016/j.electacta.2020.136764.

[34] Y. Zheng, Z. Shi, D. Guo, H. Dai, X. Han, A simplification of the time-domain equivalent circuit model for lithium-ion batteries based on low-frequency electrochemical impedance spectra, J. Power Sources 489 (2021) 229505, https://doi.org/10.1016/j.jpowsour.2021.229505.

[35] Q. Wang, Z. Hu, L. Xu, J. Li, Q. Gan, X. Du, M. Ouyang, A comparative study of equivalent circuit model and distribution of relaxation times for fuel cell impedance diagnosis, Intl. J. Energy Research 45 (2021) 15948–15961, https://doi.org/10.1002/er.6825.

[36] A. Maradesa, B. Py, E. Quattrocchi, F. Ciucci, The probabilistic deconvolution of the distribution of relaxation times with finite Gaussian processes, Electrochim. Acta 413 (2022) 140119, https://doi.org/10.1016/j.electacta.2022.140119.

[37] E. Quattrocchi, T.H. Wan, A. Belotti, D. Kim, S. Pepe, S.V. Kalinin, M. Ahmadi, F. Ciucci, The deep-DRT: a deep neural network approach to deconvolve the distribution of relaxation times from multidimensional electrochemical impedance spectroscopy data, Electrochim. Acta 392 (2021) 139010, https://doi.org/10.1016/j.electacta.2021.139010.

[38] M.B. Effat, F. Ciucci, Bayesian and hierarchical Bayesian based regularization for deconvolving the distribution of relaxation times from electrochemical impedance spectroscopy data, Electrochim. Acta 247 (2017) 1117–1129, https://doi.org/10.1016/j.electacta.2017.07.050.
[39] J. Huang, M. Papac, R. O'Hayre, Towards robust autonomous impedance spectroscopy analysis: a calibrated hierarchical Bayesian approach for electrochemical impedance spectroscopy (EIS) inversion, Electrochim. Acta 367 (2021) 137493, https://doi.org/10.1016/j.electacta.2020.137493.
[40] A. Kulikovsky, PEM fuel cell distribution of relaxation times: a method for the calculation and behavior of an oxygen transport peak, Phys. Chem. Chem. Phys. 34 (2020) 19131–19138, https://doi.org/10.1039/D0CP02094J.
[41] A. Maradesa, B. Py, T.H. Wan, M.B. Effat, F. Ciucci, Selecting the regularization parameter in the distribution of relaxation times, J. Electrochem. Soc. 170 (2023) 030502, https://doi.org/10.1149/1945-7111/acbca4.
[42] M. Žic, L. Vlašić, V. Subotić, S. Pereverzyev, I. Fajfar, M. Kunaver, Extraction of distribution function of relaxation times by using Levenberg-Marquardt Algorithm: a new approach to apply a discretization error free Jacobian matrix, J. Electrochem. Soc. 169 (2022) 030508, https://doi.org/10.1149/1945-7111/ac55c9.
[43] S.V. Pereverzev, S.G. Solodky, V.B. Vasylyk, M. Žic, Regularized collocation in distribution of diffusion times applied to electrochemical impedance spectroscopy, Comput. Methods Appl. Math. 20 (2020) 517–530, https://doi.org/10.1515/cmam-2019-0111.
[44] A. Piccioni, P. Vecchi, L. Vehcchi, S. Grandi, S. Caramori, R. Mazzaro, L. Pasquini, Distribution of relaxation times based on lasso regression: a tool for high-resolution analysis of IMPS data in photoelectrochemical system, J. Phys. Chem. C 127 (2023) 7957–7964, https://doi.org/10.1021/acs.jpcc.3c00770.
[45] D. Clematis, T. Ferrari, A. Bertei, A.M. Asensio, M.P. Carpanese, C. Nicolella, A. Barbucci, On the stabilization and extension of the distribution of relaxation times analysis, Electrochim. Acta 391 (2021) 138916, https://doi.org/10.1016/j.electacta.2021.138916.
[46] T. Paul, P.W. Chi, P.M. Wu, M.K. Wu, Computation of distribution of relaxation times by Tikhonov regularization for Li ion batteries: usage of L-curve method, Sci. Rep. 11 (2021) 12624, https://doi.org/10.1038/s41598-021-91871-3.
[47] S. Hershkovitz, S. Tomer, S. Baltianski, Y. Tsur, ISGP: impedance spectroscopy analysis using evolutionary programming procedure, ECS Trans. 33 (2019) 67–73, https://doi.org/10.1149/1.3589186.
[48] E. Tuncer, M. Wegener, R. Gerhard-Multhaupt, Distribution of relaxation times in α-phase polyvinylidene fluoride, J. Non-Cryst. Solids 351 (2005) 2917–2921, https://doi.org/10.1016/j.jnoncrysol.2005.03.055.
[49] J. Huang, N.P. Sullivan, A. Zakutayev, R. O'Hayre, How reliable is distribution of relaxation times (DRT) analysis? A dual regression-classification perspective on DRT estimation, interpretation, and accuracy, Electrochim. Acta 443 (2023) 141879, https://doi.org/10.1016/j.jnoncrysol.2005.03.055.
[50] L. Wildeuer, P. Gieler, A. Karger, Combining the distribution of relaxation times from EIS and time-domain data for parameterizing equivalent circuit models of lithium-ion batteries, Batteries 7 (2021) 3390, https://doi.org/10.1016/j.electacta.2023.141879.
[51] B.A. Boukamp, Fourier transform distribution function of relaxation times; application and limitations, Electrochim. Acta 154 (2015) 35–46, https://doi.org/10.1016/j.electacta.2014.12.059.
[52] E. Tuncer, S.M. Gubanski, On dielectric data analysis: using the Monte Carlo method to obtain relaxation time distribution and comparing non-linear spectral function fit, IEEE Trans. Dielectr. Electr. Insul. 8 (2001) 310–320, https://doi.org/10.1109/94.933337.
[53] M. Kunaver, Z. Rojec, V. Subotic, S. Pereverzyev, M. Zic, Extraction of distribution function of relaxation times by using DRT-RBLM Tools: a new approach to combine Levenberg-Marquardt algorithm and radial basis functions for discretization basis, J. Electrochem. Soc. 169 (2022) 110529, https://doi.org/10.1149/1945-7111/ac9a83.
[54] A.K. Baral, Y. Tsur, Impedance spectroscopy of Gd-doped ceria analyzed by genetic programming (ISGP) method, Solid State Ionics 304 (2017) 145–149, https://doi.org/10.1016/j.ssi.2017.04.003.
[55] F. Ciucci, C. Chen, Analysis of electrochemical impedance spectroscopy data using the distribution of relaxation times: a Bayesian and hierarchical Bayesian approach, Electrochim. Acta 167 (2015) 439–454, https://doi.org/10.1016/j.electacta.2015.03.123.
[56] J. Liu, F. Ciucci, The Gaussian process distribution of relaxation times: a machine learning tool for the analysis and prediction of electrochemical impedance spectroscopy data, Electrochim. Acta 331 (2020) 135316, https://doi.org/10.1016/j.electacta.2019.135316.
[57] J. Sherma, W.J. Morrison, Adjustment of an inverse matrix corresponding to a change in one element of a given matrix, Ann. Math. Stat. 21 (1950) 124–127, https://doi.org/10.1214/aoms/1177729893.
[58] J. Ding, A. Zhou, Eigenvalues of rank-one updated matrices with some applications, Appl. Math. Lett. 20 (2007) 1223–1226, https://doi.org/10.1016/j.aml.2006.11.016.
[59] Y. Zhuang, M. Li, Adaptive step size rules for stochastic optimization in large-scale learning, Stat. Comput. 33 (2023) 33–45, https://doi.org/10.1007/s11222-023-10218-2.
[60] A. Lasia, Electrochemical Impedance Spectroscopy and its Applications, Springer New York, New York, NY, 2014, https://doi.org/10.1007/978-1-4614-8933-7.
[61] T.H. Wan, M. Saccoccio, C. Chen, F. Ciucci, Influence of the discretization methods on the distribution of relaxation times deconvolution: implementing radial basis functions with DRTtools, Electrochim. Acta 184 (2015) 483–499, https://doi.org/10.1016/j.electacta.2015.09.097.
[62] Z. Wang, Y. Wang, L. Shen, Z. Jin, H.M. Law, A. Wang, W. Wang, F. Ciucci, Towards durable practical lithium–metal batteries: advancing the feasibility of poly-DOL-based quasi-solid-state electrolytes via a novel nitrate-based additive, Energy Environ. Sci. 16 (2023) 4084–4092, https://doi.org/10.1039/D3EE02020G.
[63] M. Mahoney, W. Micheal, P. Drineas, CUR matrix decompositions for improved data analysis, Proc. Natl. Acad. Sci. USA 106 (697) (2009), https://doi.org/10.1073/pnas.0803205106.
[64] C.E. Rasmussen, C.K.I. Williams, Gaussian Processes for Machine Learning, MIT Press, Cambridge, Mass, 2006, https://doi.org/10.7551/mitpress/3206.001.0001.
[65] N. Schilling, M. Wistuba, L. Schmidt-Thiene, Scalable hyperparameter optimization with products of Gaussian process experts, European Confer. ECML Proceedings I (2016) 33–48, https://doi.org/10.1007/s10994-017-5684-y.
[66] C.A. Pope, J.P. Gosling, S. Barber, J.S. Johnson, T. Yamaguchi, G. Feingold, P. G. Blackwell, Gaussian process modeling of heterogeneity and discontinuities using Voronoi tessellations, Technometrics 63 (2021) 53–63, https://doi.org/10.1080/00401706.2019.1692696.